# Parallel Coil Resonators for Time-Domain Radiofrequency Electron Paramagnetic Resonance Imaging of Biological Objects

N. Devasahayam, S. Subramanian, R. Murugesan, J. A. Cook, M. Afeworki,
R. G. Tschudin, J. B. Mitchell, and M. C. Krishna

*Radiation Biology Branch, Division of Clinical Sciences, National Cancer Institute, National Institutes of Health, Bethesda, Maryland 20892*

**Resonators suitable for time-domain electron paramagnetic resonance spectroscopy and imaging at a radiofrequency capable of accommodating experimental animals such as mice are described. Design considerations included $B_1$ field homogeneity, optimal $Q$, spectral bandwidth, resonator ring-down, and sensitivity. Typically, a resonator with 25-mm diameter and 25-mm length was constructed by coupling 11 single loops in parallel with a separation of 2.5 mm. To minimize the resonator ring-down time and provide the necessary spectral bandwidth for *in vivo* imaging experiments, the $Q$ was reduced predominantly by overcoupling. Capacitive coupling was utilized to minimize microphonic effects. The $B_1$ field in the resonator was mapped both radially and axially and found to be uniform and adequate for imaging studies. Imaging studies with phantom objects containing a narrow-line spin probe as well as *in vivo* objects administered with the spin probe show the suitability of these resonators for valid reproduction of the spin probe distribution in three dimensions. The fabrication of such resonators is simple and can be scaled up with relative ease to accommodate larger objects as well.** © 2000 Academic Press

## INTRODUCTION

Electron paramagnetic resonance (EPR) spectroscopy is a direct and sensitive technique for detecting paramagnetic species such as free radicals. With the increasing importance of free radicals in biology, EPR spectroscopy is used to understand the basic mechanisms of several disease processes with putative free radical pathways (*1*). EPR imaging can be implemented for *in vivo* biological studies (*2*), using physical principles similar to those of magnetic resonance imaging (MRI) (*3*). Recent studies have reported on the EPR imaging of intact objects such as isolated organs as well as experimental animals to detect endogenously generated free radicals as well as the spatial distribution of exogenously administered free radicals (*4–9*). Such experiments have established the capability of EPR imaging to provide valuable physiological information such as tissue oxygen status as well as tissue redox status (*5, 10, 11*). Obtaining such information noninvasively is of importance in characterizing pathological states as well as guiding effective treatments, making EPR imaging a poten-

tially useful tool in diagnostic radiology (*10*). Several studies have obtained useful physiological information using spin probes such as nitroxides and particulates such as glucose char and India ink, (*8, 12–14*). The linewidths of these compounds are in the 0.5–5 G range requiring the use of continuous wave (CW) EPR detection since the transverse relaxation time $T_2$ is in the order of 250–50 ns.

With the recent availability of biologically compatible, nontoxic, water-soluble spin probes exhibiting a single-line EPR spectrum with oxygen-dependent linewidth in the range of 50–200 mG, time-domain EPR techniques are receiving increasing attention because of the sensitivity inherent to the pulsed EPR techniques as well as minimal artifacts associated with object motion (*15–19*). In addition, substantially shorter times for a three-dimensional imaging experiment (<5 min) compared to CW EPR imaging (25–30 min) make it possible to collect several three-dimensional images after administration of the spin probe and thereby allow monitoring of pharmacokinetic data. The feasibility of performing *in vivo* imaging experiments using time-domain radiofrequency (RF) EPR has been shown at 300 MHz by administering water-soluble triarylmethyl (TAM)-based paramagnetic spin probes to mice and examining regional anatomies (*16*). Subsequent efforts have been directed to: (1) provide capability to study whole animals (*17*); and (2) evaluate receiver configurations and data acquisition methodologies to enhance sensitivity (*20*). In this paper, design considerations for a resonator capable of accommodating an experimental animal such as a mouse are described with emphasis on B1 field homogeneity, minimization of dead time, efficient utilization of RF power, and optimal spectral bandwidth. Imaging data from phantom objects and from *in vivo* experiments are presented.

## RESONATOR DESIGN CONSIDERATION

### *Resonator Ring-Down Time, Sensitivity, and Spectral Bandwidth*

For the detection of a paramagnetic spin probe with pulsed EPR, the time-domain response after a pulsed excitation should

be longer than the recovery time of the spectrometer. The recovery time of a time-domain EPR spectrometer depends on the resonator ring-down time and the receiver recovery time associated with the overload of the preamplifier. A parallel resonant circuit with inductance $L$, capacitance $C$, and resistance $R$ has a ringing transient of angular frequency $\omega_r$ and decay time constant $\tau_r$ given, respectively, by

$$\omega_r = \omega_0[1 - 1/(4Q^2)]^{0.5} \qquad [1]$$

and

$$\tau_r = 2Q/\omega_0, \qquad [2]$$

where $\omega_0 = (LC)^{-0.5}$ and $Q = R/(\omega_0 L)$. For an 80-W RF pulse input, about 16 time constants of $\tau_r$ are required for the ringing transient to decay below the level of the time-domain response of the spin probe to permit detection. Hence the receiver dead time may be approximately given by (21)

$$\tau_d \sim 32Q/\omega_0. \qquad [3]$$

The dead time is inversely related to the carrier frequency (Eq. [3]) and hence might be a serious problem for the successful detection of the time-domain responses at RF from spin probes which have spin–spin relaxation times ($T_2$) less than 1 $\mu$s. For a resonator tuned to 300 MHz with a $Q$ of 25 and a bandwidth of 12 MHz, following the trailing edge of the RF pulse of 80-W peak power, the receiver will be in the overload condition and hence will be "dead" for about 425 ns. Therefore, unlike at X-band and higher frequencies, where time-domain responses from nitroxides have been collected using high $Q$ cavity resonators, detection of EPR signals from fast relaxing spin probes might not be feasible at RF frequencies. Similar reasons preclude the use of high $Q$ resonators typically used in MRI. However, $Q$ cannot be significantly lower since the SNR (signal to noise ratio) is proportional to $Q$ as well and is given by

$$SNR \propto (VQ)^{0.5}, \qquad [4]$$

where $V$ is the resonator volume.

The SNR spectrum obtained from a signal-averaged free induction decay (FID) is given by (22)

$$SNR\alpha(2MNKQ)^{0.5}\exp(-\tau_d/T_2^*), \qquad [5]$$

where $M$ is the number of samples in an FID, $N$ is the number of FIDs averaged, $K$ is the duty cycle of the receiver, $\tau_d$ is the dead time, and $T_2^*$ is the spin–spin relaxation time of the spin probe. From Expression [5], it can be seen that SNR is directly related to $Q^{0.5}$ and inverse exponentially related to $\tau_d$. Therefore, the decrease in SNR by using lower $Q$ might be more than

compensated by the reduced dead time. Additionally, optimal $Q$ of a resonator might be determined by the spectral properties of the paramagnetic spin probe being investigated and is given by (23)

$$Q_{opt} = \omega_0(T_2^*/64). \qquad [6]$$

For a homogeneously broadened Lorentzian EPR absorption,

$$T_2^* = 1/\pi\Delta B, \qquad [7]$$

where $\Delta B$ is the linewidth of the resonance, expressed in frequency units (for free radicals with $g = 2$, 1 G = 2.8 MHz). For an EPR probe with a linewidth of 150 mG (typical of the TAM radicals), $T_2^*$ becomes 760 ns, thereby requiring $Q_{opt}$ to be approximately 22. For resonators with $Q$ ranging between 20 and 25 and using a gradient of 1 G/cm in imaging experiments, the spectral bandwidth will be in the range of 12–15 MHz, providing the capability of imaging an object of 4-cm maximum linear dimension. Based on these factors, cylindrical resonators of 25-mm bore size and 25- to 50-mm length, with $Q$ in the range of 20–25, have been chosen to accommodate experimental animals such as mice and study the distribution of spin probes with time-domain responses lasting for >1 $\mu$s. NMR probes with recovery times in the order of 10 $\mu$s have been constructed by connecting two interspersed solenoidal coils in parallel (24, 25). In such a configuration at a given frequency, these probes provide larger volume than single-coil probes. The minimization of dead time in these coils has been attributed to the reduced inductance. While similar resonators were used successfully in time-domain EPR imaging to image small volumes *in vivo* (16), this design was found to be not suitable for studies of larger objects by keeping the inductance low. Recently a submicrosecond resonator and receiver system for time-domain EPR imaging at radiofrequency has been described (26). This resonator could accommodate a maximum volume of 55 ml. With the RF power available, pulses of 300 ns duration were used for excitation of a phantom object filled with 1.5 g lithium phthalocyanine containing $10^{21}$ spins as a biomimetic phantom and imaging experiments were carried out. However, such resonators might need larger bandwidth (governed by pulse width and $Q$) to image intact biological objects. The resonators described in this study, consisting of several individual conducting elements coupled in parallel, have optimal sensitivity, acceptable $B_1$ field homogeneity, and short ring-down time, enabling whole-body imaging of a mouse.

## EXPERIMENTAL

### Spectrometer

The technical details of the time-domain RF EPR imaging spectrometer have been published elsewhere (17, 20). Briefly,

the spectrometer consists of a transmitting arm, a receiving arm, and a resonator. RF pulses are delivered from the transmitting arm to the resonator through a diplexer. The transmitting arm consists of a 300-MHz frequency source which is derived from an 800-MHz oscillator. The 300 MHz is properly gated to obtain pulses of required width, depending on the resonator volume. Pulse widths typically ranged between 45 and 160 ns. The pulse-modulated 300-MHz radiation is amplified by two class A 100-W amplifiers. The outputs from the amplifiers were combined to obtain 160 W and delivered to the resonator through the diplexer; a 3-dB loss at the diplexer results in net power of 80 W at the resonator. The receiving arm collects the time-domain responses from the spin probe in the resonator after the receiver gate was opened 450 ns after the delivery of the power to the resonator. By this time the major part of the ringing gets diminished to a level at which the signal from the spin probe can be recovered. However, the small systematic ringing, present in the region of 450–650 ns, can be further minimized from the acquired FID by subtracting it from a signal collected in the absence of magnetic field. This brings down the overall dead time from 650 to 450 ns. The signal received at 300 MHz is amplified and mixed with a frequency of 350 MHz derived from the same 800-MHz source to obtain an intermediate frequency (IF) signal at 50 MHz containing the FID. The output from the mixer which is centered around 50 MHz is digitized by the 1 GS/s two-channel Analytek digitizer. For signal averaging, alternate pulses were applied 180° out-of-phase with each other and the resulting responses were combined to reduce the systematic buildup of the spectrometer noise. The details of the digitizer/averager in the IF configuration have been described elsewhere (20).

## Resonator Construction

Figure 1A provides the electrical schematic diagram depicting the various components of the resonator. For example a resonator of 25-mm diameter was constructed with 11 coil elements, 2.5 mm apart to give a 25-mm height. The inductance of each individual coil was measured to be 0.0936 $\mu$H. Under the absence of mutual coupling, the total inductance would be 0.0085 $\mu$H. However, the experimentally measured inductance was 0.049 $\mu$H, due to mutual inductance between individual coil elements (27). With the capacitance values of C1 = 9.58 pF, C2 = 9.779 pF, and C3 = 14.26 pF, the resonator could readily be tuned to the operating frequency of 300 MHz.

*Longitudinal $B_1$ field.* Figure 1B provides schematics of the coil positioning and winding. The resonator was built by winding and supporting individual coil elements (AWG 26 silver wire with circular cross section) on a lucite mandrel. The diameter of the individual loops and the length of the connecting leads were maintained equal to minimize phase errors in the RF energy delivered to the resonator. The interior of the coil was used to house the sample such that the cylindrical axis
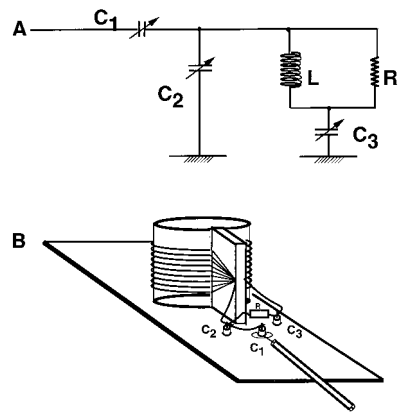


**FIG. 1.** (A) The components of the LCR circuit that make up the resonator assembly. The values of C1 (tuning capacitor), C2 (coupling capacitor), and C3 (matching capacitor) depend on the frequency and dimensions of the coil. (B) Schematics of the parallel coil resonator with the RF magnetic axis coaxial with the cylindrical axis. This configuration will be useful for phantom studies, but will require loading small animals in a vertical orientation in a horizontal $B_0$ field.

of the resonator is maintained perpendicular to $B_0$. The connecting leads of the resonator to the tuning and matching capacitors were supported by a dielectric supporter which acts as insulation between the input and output leads. The resulting structure and the tuning and matching capacitors were mounted on a copper-coated glass epoxy board. The resonator was energized through a semirigid cable.

*Transversal $B_1$ field.* Resonator design supporting homogenous fields transverse to the cylindrical axis of the probe permits access to the active volume of the resonator along the axis of the main magnet; such a configuration is desirable for *in vivo* imaging experiments. A resonator with such a configuration can be constructed by winding the individual conducting elements running along the long axis of the lucite tube.

The resonators are shielded with a copper sheet to reduce RF interference from extraneous sources. Several axial and vertical resonators with diameter in the range 15–50 mm and length in the range 15–80 mm were constructed and tested. The 900 pulse width at an RF power of 80 W varied between 45 and 160 ns for the active volume ranging from 8 to 100 cm³. In this paper, however, we present the results from the longitudinal $B_1$ field resonators. The transverse $B_1$ field resonator configuration will, of course, permit an easier handling of the animal. A technical evaluation of such a resonator, its size–frequency relationship, and comparison with bird cage resonators of comparable size, etc., are yet to be carried out and will be reported subsequently.

## RESULTS

### Resonator Characteristics

*Bandwidth.* For a field gradient of 1.5 G/cm, the spatial dimensions of a 25 × 25 mm resonator sets an upper limit of
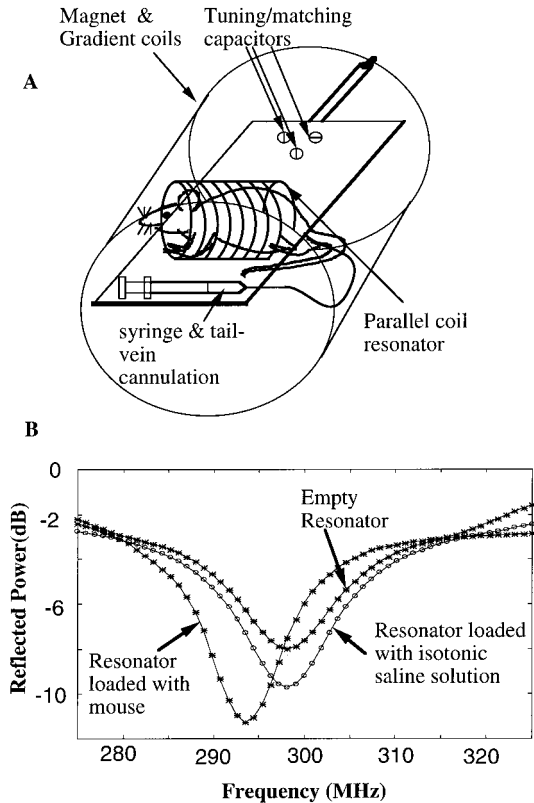
**FIG. 2.** (A) Cartoon of a mouse placed in the parallel coil resonator. The dimensions of the coil used in murine studies allow the placing of the animal transverse to the field and infusion of drugs and anesthetics while the animal is inside the assembly. (B) The RF reflectance profiles of the $25 \times 25$ mm parallel coil resonator tuned to 300 MHz with an overcoupled $Q$ of around 20. It can be seen that loading the resonator to nearly 90% capacity with saline solution does not change the $Q$ or the frequency appreciably. In presence of the mouse a marginal increase in $Q$ was observed.

28.5 to the $Q$ of the resonator, governed by the spectral bandwidth of 10.5 MHz, when the resonator is tuned to 300 MHz. $Q$ can be reduced to the desired value either by resistive damping or by capacitive overcoupling. It has been observed that, for the same RF power, higher $B_1$ fields are achieved for overcoupling (28). For example, the ratio of the signal intensities from an overcoupled resonator to a matched resonator ($Q$-spoiled) is given by

$$S_{(overcoupled)}/S_{(matched)} = [2\beta/(1 + \beta)]^{0.5}, \qquad [8]$$

where $\beta$ is the coupling coefficient (21). Hence, in the present study, $Q$ damping was carried out by capacitive overcoupling primarily. Additionally, a resistance (3.3 kohm) in parallel was used to reduce $Q$ whenever it was not possible by solely overcoupling. Figure 2A shows the typical arrangement for *in vivo* experiments as well as phantom imaging studies. The resonator is placed in the active volume of the magnet/gradient

coil assembly. Figure 2B shows the $Q$-profiles of an empty resonator tuned to 300 MHz, when adjusted to a spectral bandwidth of 15 MHz. Figure 2B also shows the effect of loading the resonator with 20 ml saline solution and a live mouse of 20 g body wt. From the $Q$-profiles, it can be seen that the resonator is sufficiently overcoupled such that there was no significant loading either by saline solution or by the animal itself. In fact, a slight increase in $Q$ was observed when the animal was placed in the resonator. The $Q$ was readjusted back to 20 to maintain the desired spectral bandwidth.

*Ring-down time.* Figure 3A shows the signal (an average of 100,000 time-domain responses) when a 80-W RF pulse of 70 ns duration was delivered to a 50-ohm dummy load. The ring-down time, which can be attributed to the spectrometer recovery independent of the resonator, was found to be approximately 500 ns. Figure 3B shows the ring-down time of the parallel coil resonator tuned and matched to 300 MHz when a transmit pulse of 80 W of identical duration was delivered. With a resonator of $Q$ 20, a ring-down time of nearly 650 ns was observed in contrast to the 500 ns observed for the 50-ohm termination. This result suggests that an additional 150 ns is contributed to the receiver recovery by the parallel coil resonator. This recovery time might be reduced further using pulses of shorter width or by active damping (26).
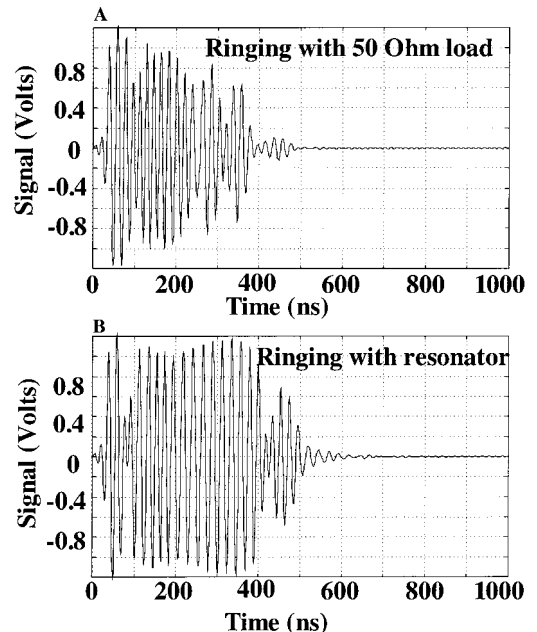


**FIG. 3.** (A) The plot of the receiver response after a 70-ns pulse (80 W) was transmitted to a 50-ohm load. The receiver gate was opened immediately after the transmit pulse. It can be seen that the ringing of the circuit, inclusive of preamplifier recovery, is around 500 ns. (B)The receiver response as in (A), but this time the 50-ohm load is replaced by the parallel coil resonator of $Q$ around 20. It can be seen that the ringing time has now increased to a total of 650 ns after the trailing edge of the pulse. In both the figures, the *x*-axis origin corresponds to time "zero" after the transmit pulse.

*RF field.* The flip angle in a single pulse experiment is given by

$$\theta = \gamma B_1 t_p, \qquad [9]$$

where $t_p$ is the RF pulse duration in seconds, $B_1$ is the RF magnetic field flux density in Gauss, and $\gamma$ is the gyromagnetic ratio, $1.7608 \times 10^7$ radians/s/G for a $g = 2$ species. For an 80-W RF pulse (70 ns) corresponding to a 90° pulse delivered to the resonator (matched as a 50-ohm load), the reflected power was measured to be 8 W, which corresponds to a net input of 72 W. The flux density calculated from these values corresponds to a $B_1$ field of 1.2 G. $B_1$ can also be calculated from the inductance and the current and is given by

$$B_1(T) = \text{current (Amp)} \times (\text{inductance } (H)/\text{coil area } (m^2)). \qquad [10]$$

From the measured inductance of 0.049 $\mu$H for the coil and the coil dimensions (25 mm diameter), the $B_1$ field is calculated to be 1.76 G, which is comparable to that computed from the pulse width and the power.

*RF field distribution.* Homogeneity and magnitude of the RF field in the resonator are critical factors for EPR imaging. In order to examine the $B_1$ field homogeneity in the parallel coil resonator prior to imaging experiments, EPR spectral intensities of a point source paramagnetic species were measured at various locations in the resonator. The solid charge-transfer complex, *N*-methylpyridinium tetracyanoquinodimethane (NMP-TCNQ), occupying a total volume of ~5 $\mu$l, with its EPR spectrum consisting of a single narrow line with width of approximately 200 mG, was used (see Figs. 4A and 4B). The volume occupied by NMP-TCNQ was therefore maintained less than the expected spatial resolution in the EPR image with the gradient strength used in imaging experiments and hence could be considered as a point source. By moving this point source radially and axially in steps of 1.5 mm, EPR spectra were collected at each location to map the $B_1$ field. The variation of the spectral intensity of this point source was <10% axially and <5% radially within the volume of the cylindrical resonator. A radial profile of the $B_1$ field in the middle of the resonator is shown in Fig. 4C. However, in the presence of imaging gradients the spectral profile is to be corrected using $Q$-profile of the coil depending upon the frequency bandwidth. This has a characteristic Gaussian profile centered around the carrier frequency. The so-called $Q$-profile can be mapped and was used to correct any offset dependent intensity changes in the images.

### 3D Imaging Experiments

*Phantom imaging.* In order to test the imaging capabilities of the parallel coil resonators, phantom objects containing spin
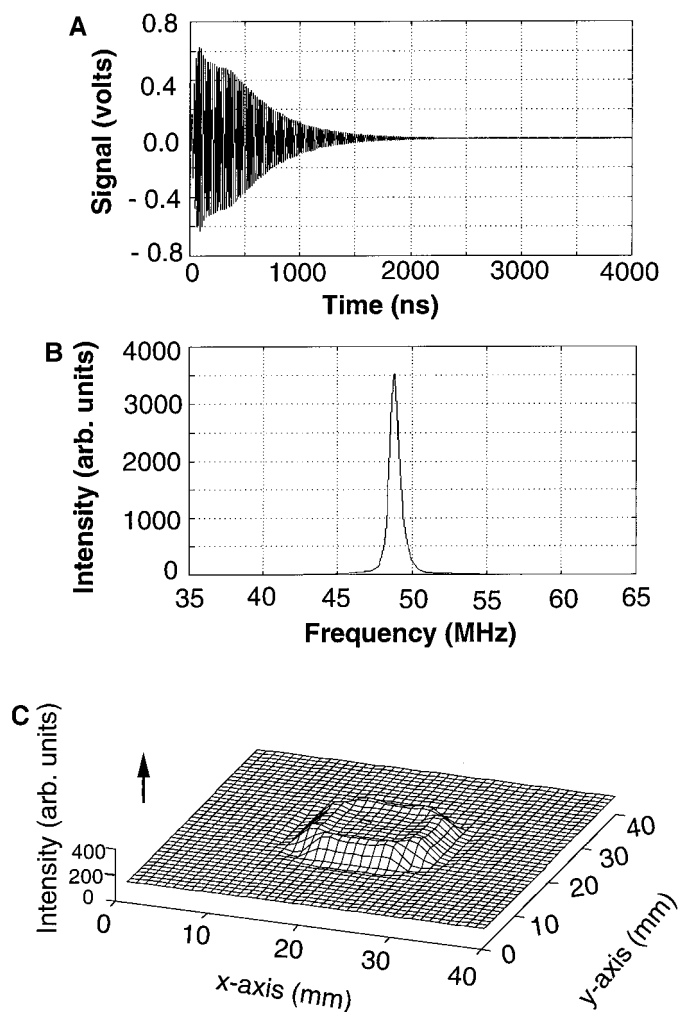


**FIG. 4.** (A) The FID of a sample of TCNQ occupying a volume of 5 $\mu$L at the center of a 25 × 25 mm parallel coil resonator following a 900 pulse. The $Q$ of the resonator was 20. A total of 100,000 FIDs of 4 K record length, collected at a sampling rate of 1 Gs/s, were averaged (averaging time, 2 s). The averaged FID shows an effective dead time of 450 ns after the background subtraction. (B) Fourier transform of the FID in (A) after apodization with a Kaiser filter of order 5. The magnitude mode of the spectrum ($sqrt (u^2 + v^2)$) is shown, and this has a linewidth of 250 mG. (C) Using the above point source of TCNQ the RF flux density was mapped in a radial plane at the middle of the resonator perpendicular to the axis. This is shown as a 3D profile, with the horizontal axis representing the measurement plane and the vertical axis the RF flux density in terms of the EPR line intensity. The RF flux was found to be uniform within 5% of the mean.

probes distributed in defined physical configurations were employed. One of the phantoms reported here is composed of a lucite cylinder of 25-mm diameter which fits snugly in the parallel coil resonator. The schematics of the phantom and the laboratory axes are shown in Fig. 5A. Two holes (4 mm diameter) drilled in the lucite cylinder were filled with the water-soluble spin probe TAM (1 mM) for imaging studies. The chemical structure and spectral properties of TAM are described in (*29*). The spectrum of TAM at 300 MHz consists
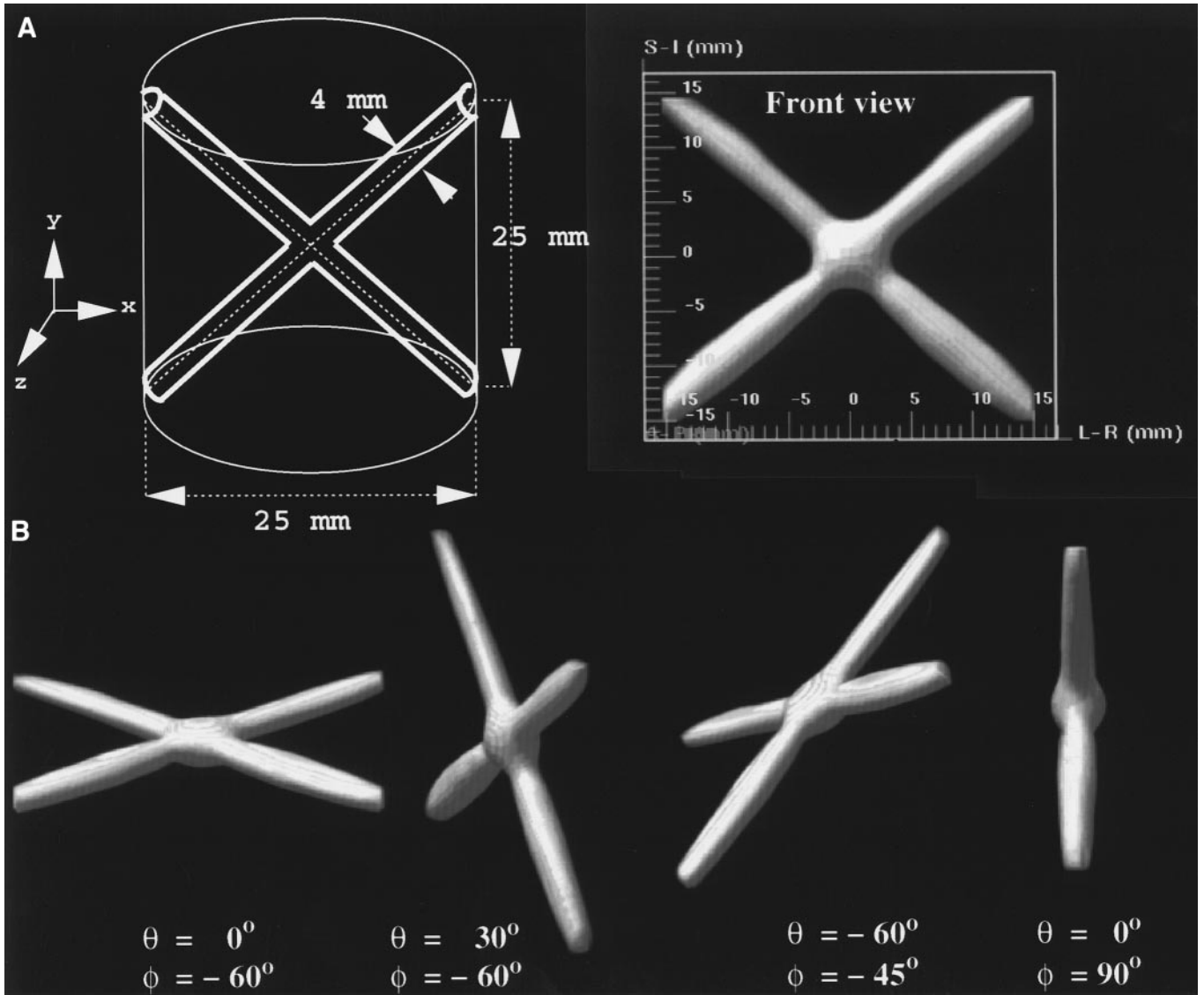
**FIG. 5.** The 3D imaging performance of the longitudinal parallel coil resonator is summarized. The phantom consisted of a planar X-shaped drilling with the holes of the X-shape bisecting the $y$ and $z$. The holes were filled with 800 $\mu$L 1 mM TAM in saline solution and were imaged with the gradient vector spanning the polar and azimuthal dimensions in steps of 15° corresponding to a total of 144 projections. The gradient was 1.2 G/cm and the linewidth of the spin probe in the absence of the gradient was 170 mG. The three dimensional images obtained after filtered back-projections are shown at some specific orientations. In this figure, the $y$-axis is the polar axis and the $xz$-plane is the azimuthal plane. The surface rendering is done using Voxelview in a Silicon Graphics Indigo2 workstation.

of a single narrow line at $g = 2$, with a Lorentzian absorption linewidth of 170 mG. When the FIDs are processed in magnitude mode this increases to 250 mG due to the admixture of absorption and dispersion signals. The FID lasts up to 2600 ns when the receiver gate was opened 600 ns following the trailing edge of the excitation pulse. This agrees with a $T_2^*$ of 670 ns calculated from the linewidth and the total expected duartion of the FID of ~3300 ns. It should be mentioned, however, that the duration of FID that can be acquired under imaging gradients of 1.2 G/cm is under 1000 ns due to the shortened $T_2^*$. With pulses of 70 ns width, image data were collected by summing 100,000 FIDs per projection. For each projection, 4 K points of FIDs were collected after a dead-time delay of approximately 600 ns with a sampling rate of 1Gs/s. The imaging gradient vector of amplitude 0.8 G/cm was oriented equally dispersed with the polar and azimuthal angles ($\theta$ and $\phi$) varying in equal steps of 15 corresponding to a total of 144 projections. The resulting time-domain signals were filtered using a digital Butterworth filter with a passband of 20 MHz centered around 50 MHz (zero-gradient resonance frequency), apodized using a Kaiser filter of order 5 and zero-filled to 32 or 64 K before Fourier transform (FT). The spectra
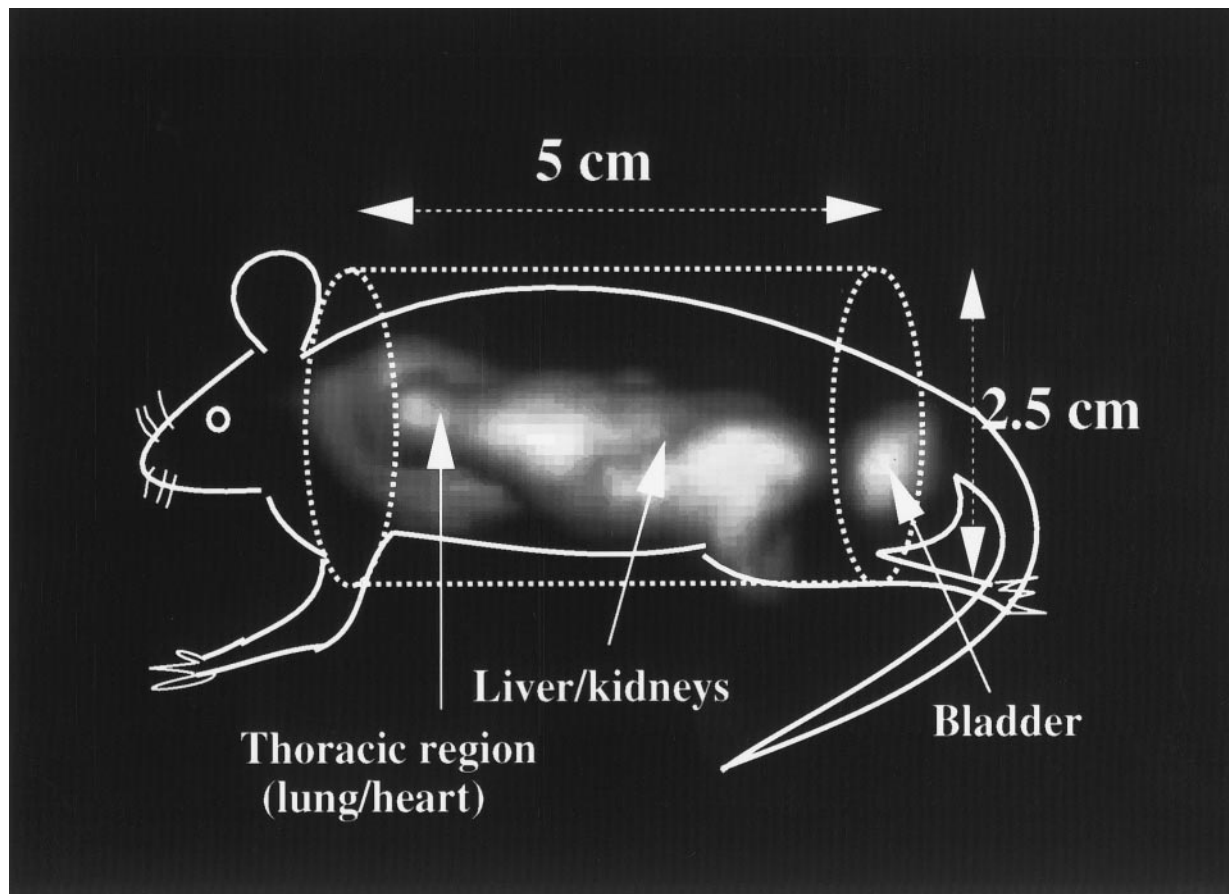
**FIG. 6.** Three dimensional EPR imaging of C3H mouse administered intravenously with the TAM spin probe (100 $\mu$l, 20 mM). The image collection was initiated immediately after the infusion of the spin probe. Prior to imaging, the animal was anesthetized using ketamine/xylazine mixture and placed in the resonator. The resonator sampled the animal from the neck to pelvic regions as shown in the cartoon. EPR projection data were collected using a gradient of 1 G/cm. The three dimensional image was obtained by filtered back-projection methods.

after FT were taken in absolute value mode for image processing. The frequency range of all the projections corresponding to the volume of interest was adjusted to be within 128 or 256 points of an image window centered around 50 MHz in the digitized spectrum and used for image reconstruction using filtered back-projection. The resulting images were surface rendered using Voxelview in a Silicon Graphics Indigo2 workstation. The various perspectives of the images obtained are shown in Fig. 5B. The images correspond well with the physical dimensions of the phantom and represent the uniform distribution of the spin density. These results from the phantom studies suggest that the parallel coil resonators are suitable for detecting and imaging spin probe distribution in biological objects, provided that: (1) the spins have their time-domain response lasting longer than the resonator ring-down time (650 ns); (2) the spin probe distribution can be spatially encoded with gradients of appropriate strength so as to accommodate the signals within the bandwidth provided by the resonator; and (3) adequate concentration of the spin probes is available in the resonator to achieve satisfactory SNR.

*In vivo imaging.* In order to test the feasibility of using the parallel resonator for *in vivo* imaging, an anesthetized mouse was placed in a 25 × 50 mm resonator after tail vein cannulation. The resonator was placed in the magnet/gradient assembly as shown in Fig. 2A. The animal was intravenously administered with a 100-$\mu$l solution of a 20-mM TAM in isotonic saline and the data collection was initiated. The FIDs were collected and processed as outlined above. The image of the spin probe distribution obtained from the mouse is shown in Fig. 6. Based on the placement of the animal in the parallel coil and the images obtained, several areas in the thoracic, abdominal, and pelvic regions could be recognized. The absence of image intensity from other regions could be a result of inadequate accumulation of the spin probe or faster relaxing time-domain responses corresponding to well-oxygenated regions. Based on the linewidth of the spin probe, resolution of the image was found to be in the millimeter range, consistent with the gradients used. These results suggest that the parallel coil resonator provides valid representation of the spin probe *in vivo.*

## DISCUSSION

*In vivo* EPR spectroscopy and imaging, with the use of exogenous spin probes, have been employed to obtain valuable physiological information such as tissue oxygen and redox status (*4–9*). Such information has been monitored as a function of treatment procedures to guide effective treatments as well (*10*). These studies together have validated the capabilities of EPR imaging as a potentially useful functional imaging modality. Most of these studies have used CW EPR methods where resonators of the loop–gap type (*4, 5, 30*), surface coil (*31*), or reentrant configuration (*6*) were advantageous to enhance sensitivity. Recently available narrow-line spin probes (*16, 29, 32, 33*) which are water soluble and nontoxic have provided the capability for EPR imaging to obtain high-resolution spatial images. Moreover, these agents are amenable for *in vivo* studies with time-domain EPR imaging (*17*). Several factors need to be considered in the development of resonators for time-domain EPR imaging methodology for *in vivo* applications. While in MRI, the frequency bandwidth is in the order of <20 kHz to obtain high-resolution images of large-size objects, in EPR the required bandwidth is at least 10 MHz even for a resonator of 25-mm bore size. Desirable features of a resonator for such time-domain EPR applications are: (1) ability to accept narrow and intense pulses and convert to $B_1$ efficiently; (2) short resonator ring-down time; (3) optimal $Q$-profiles with adequate spectral bandwidth for imaging studies; (4) adequate $B_1$ field homogeneity; and (5) ability to be scaled up for larger objects. When field gradients of 1 G/cm are used, a spectral band width of at least 10–12 MHz is needed. Therefore, pulses of width no more than 100 ns should be used to provide an excitation bandwidth of 10–12 MHz. The pulsed RF EPR images obtained from phantoms of defined physical architecture containing the spin probes show good correspondence in terms of the dimension as well as uniformity of image intensity. *In vivo* pulsed RF EPR imaging experiments from mice administered with the spin probe could, in principle, provide images with resolution in the millimeter range. The present study shows that pulsed RF EPR imaging can be performed in live objects of moderate size and important physiological information can be collected. The parallel coupling of coil elements enables the scaling up of the volume without a significant increase in the overall inductance. This helps in the construction of large-volume resonators at frequencies around 200–300 MHz without drastic changes in the values of the tuning and matching capacitors. The use of a judicious combination of overcoupling and resistive damping produces the desired low $Q$, short dead-time, and broad bandwidth required in resonators for pulsed RF EPR imaging of intact biological objects. In this article, the parallel coil resonators which have been described and evaluated for *in vivo* imaging may well be an attractive alternative to bird-cage, solenoidal, and loop–gap resonators in magnetic resonance imaging. The $B_1$ field homogeneity has been found to be suitable for performing three-dimensional imaging experiments. The current resonator design is of particular advantage for studying large-size objects because the usable volume can be readily increased and the construction is inexpensive and relatively simple to fabricate.

## ACKNOWLEDGMENTS

## REFERENCES

1. B. Halliwell and J. M. C. Gutteridge, "Free Radicals in Biology and Medicine," Oxford University Press, Oxford, pp. 416–509 (1989).

2. J. L. Berliner and H. Fujii, Magnetic resonance imaging of biological specimens by electron paramagnetic resonance of nitroxide spin labels, *Science* **227**, 517–519 (1985).

3. P. C. Lauterbur, Image formation by induced local interactions: Examples employing nuclear magnetic resonance, *Nature* **242**, 190–191 (1973).

4. H. J. Halpern, D. P. Spencer, J. van Polen, M. K. Bowman, A. C. Nelson, E. M. Dowey, and B. A. Teicher, Imaging radio frequency electron-spin-resonance spectrometer with high resolution and sensitivity for in vivo measurements, *Rev. Sci. Instrum.* **60**, 1040–1050 (1989).

5. P. Kuppusamy, M. Chzhan, K. Vij, M. Shteynbuk, D. J. Lefer, E. Giannella, and J. L. Zweier, Three-dimensional spectral-spatial EPR imaging of free radicals in the heart: A technique for imaging tissue metabolism and oxygenation, *Proc. Natl. Acad. Sci. USA* **91**, 3388–3392 (1994).

6. M. Alecci, S. Della Penna, A. Sotgiu, L. Testa, and I. Vannuci, Electron paramagnetic resonance spectrometer for three dimensional in vivo imaging at very low frequencies, *Rev. Sci. Instrum.* **63**, 4263–4270 (1992).

7. H. Utsumi, E. Muto, S. Masuda, and A. Hamada, In vivo ESR measurement of free radicals in whole mice, *Biochem. Biophys. Res. Commun.* **172**, 1342–1345 (1990).

8. K. J. Liu, P. Gast, M. Moussavi, S. W. Norby, N. Vahidi, T. Walzak, M. Wu, and H. M. Swartz, Lithium phthalocyanine: A probe for electron paramagnetic resonance oximetry in viable biologic systems, *Proc. Natl. Acad. Sci. USA* **90**, 5438–5442 (1993).

9. H. Togashi, H. Shinzawa, T. Ogata, T. Matsuo, S. Ohno, K. Saito, N. Yamada, H. Yokoyama, H. Noda, K. Oikawa, and H. T. T. Kamada, Spatiotemporal measurement of free radical elimination in the abdomen using an in vivo ESR-CT imaging system, *Free Rad. Biol. Med.* **25**, 1–8 (1998).

10. F. Goda, J. A. O'Hara, E. S. Rhodes, K. J. Liu, J. F. Dunn, G. Bacic, and H. M. Swartz, Changes in oxygen tension in experimental tumors after a single dose of x-ray irradiation, *Cancer Res.* **55**, 2249–2252 (1995).

11. H. J. Halpern, C. Yu, M. Peric, E. Barth, D. J. Grdina, and B. A. Teicher, Oximetry deep in tissues with low-frequency electron paramagnetic resonance, *Proc. Natl. Acad. Sci. USA* **91**, 13047–13051 (1994).

12. C. S. Lai, L. E. Hopwood, J. S. Hyde, and S. Lukiewicz, ESR studies of O2 uptake by Chinese hamster ovary cells during the cell cycle, *Proc. Natl. Acad. Sci. USA* **79**, 1166–1170 (1982).

13. J. L. Zweier, M. Chzhan, U. Ewert, G. Schneider, and P. Kuppusamy, Development of a highly sensitive probe for measuring oxygen in biological tissue, *J. Magn. Reson. B* **105,** 52–57 (1994).

14. B. Gallez, R. Debuyst, F. Dejehet, K. J. Liu, T. Walczak, F. Goda, R. Demeure, H. Taper, and H. M. Swartz, Small particles of fusinite and carbohydrate chars coated with aqueous soluble polymers: Preparation and applications for in vivo EPR oximetry, *Magn. Reson. Med.* **40,** 152–159 (1998).

15. J. Bourg, M. C. Krishna, J. B. Mitchell, R. G. Tschudin, T. J. Pohida, W. S. Friauf, P. D. Smith, J. Metcalfe, F. Harrington, and S. Subramanian, Radiofrequency FT EPR spectroscopy and imaging, *J. Magn. Reson.* **102,** 112–115 (1993).

16. R. Murugesan, J. A. Cook, N. Devasahayam, M. Afeworki, S. Subramanian, R. Tschudin, J. H. A. Larsen, J. B. Mitchell, A. Russo, and M. C. Krishna, In vivo imaging of a stable paramagnetic probe by pulsed-radiofrequency electron paramagnetic resonance spectroscopy, *Magn. Reson. Med.* **38,** 409–414 (1997).

17. R. Murugesan, M. Afeworki, J. A. Cook, N. Devasahayam, R. Tschudin, J. B. Mitchell, S. Subramanian, and M. C. Krishna, A broadband pulsed radio frequency electron paramagnetic resonance spectrometer for biological applications, *Rev. Sci. Instrum.* **69,** 1869–1876 (1998).

18. A. Coy, N. Kaplan, and P. T. Callaghan, Three-dimensional pulsed ESR imaging, *J. Magn. Reson. A* **121,** 201–205 (1996).

19. M. Alecci, J. A. Brivati, G. Placidi, and A. Sotgiu, A radiofrequency (220 MHz) Fourier transform EPR spectrometer, *J. Magn. Reson.* **130,** 272–280 (1998).

20. S. Subramanian, R. Murugesan, N. Devasahayam, J. A. Cook, M. Afeworki, T. Pohida, R. G. Tschudin, J. B. Mitchell, and M. C. Krishna, High-speed data acquisition system and receiver configurations for time-domain radiofrequency electron paramagnetic resonance spectroscopy and imaging, *J. Magn. Reson.* **137,** 379–388 (1999).

21. S. Pfenninger, W. Froncisz, J. Forrer, J. Luglio, and J. S. Hyde, General method for adjusting the quality factor of EPR resonators, *Rev. Sci. Instrum.* **68,** 4857–4865 (1995).

22. J. Gorcester and J. H. Freed, Two dimensional fourier transform ESR correlation spectroscopy, *J. Chem. Phys.* **88,** 4678–4693 (1986).

23. J. Gorcester, G. L. Millhauser, and J. H. Freed, Two-dimensional electron spin resonance, In "Modern Pulsed and Continuous-Wave Electron Spin Resonance" (L. Kevan and M. K. Bowman, Eds.), Wiley, New York, pp. 119–194 (1990).

24. G. C. Chingas, Overcoupling NMR probes to improve transient response, *J. Magn. Reson.* **54,** 153–157 (1983).

25. S. B. W. Roeder, E. Fukushima, and A. A. V. Gibson, NMR coils with segments in parallel achieve higher frequencies or larger sample volumes, *J. Magn. Reson.* **59,** 307–317 (1984).

26. M. Alecci, J. A. Brivati, G. Placidi, L. Testa, D. J. Lurie, and A. Sotgiu, A submicrosecond resonator and receiver system for pulsed magnetic resonance with large samples, *J. Magn. Reson.* **132,** 162–166 (1998).

27. C. G. Fry, J. H. Iwamiya, T. M. Apple, and B. C. Gerstein, Doubly wound coils for solid-state double resonance and multiple pulse NMR, *J. Magn. Reson.* **63,** 214–216 (1985).

28. G. A. Rinard, R. W. Quine, S. S. Eaton, G. R. Eaton, and W. Froncisz, Relative benefits of overcoupled resobators vs inherently low-Q resonators for pulsed magnetic resonance, *J. Magn. Reson. A* **108,** 71–81 (1994).

29. J. H. Ardenkjaer-Larsen, I. Laursen, I. Leunbach, G. Ehnholm, L.-G. Wistrand, J. S. Petersson, and K. Golman, EPR and DNP properties of certain novel single electron contrast agents intended for oximetric imaging, *J. Magn. Reson.* **133,** 1–12 (1998).

30. W. Froncisz and J. S. Hyde, The loop gap resonator: A new lumped circuit ESR sample structure, *J. Magn. Reson.* **47,** 515–521 (1982).

31. M. Ono, K. Ito, N. Kawamura, K. Hsieh, H. Hirata, N. Tsuchihashi, and H. Kamada, A surface-coil-type resonator for in vivo ESR measurements, *J. Magn. Reson. B* **104,** 180–182 (1994).

32. K. Golman, I. Leunbach, J. H. Ardenkjaer-Larsen, G. J. Ehnholm, L. G. Wistrand, J. S. Petersson, A. Jarvi, and S. Vahasalo, Overhauser-enhanced MR imaging (OMRI), *Acta Radiol.* **39,** 10–17 (1998).

33. P. Kuppusamy, P. H. Wang, M. Chzhan, and J. L. Zweier, High resolution electron paramagnetic resonance imaging of biological samples with a single line paramagnetic label, *Magn. Reson. Med.* **37,** 479–483 (1997).